CrossMark

On the Space-Time Structure of Sheared Turbulence

Martin de Maré[1] · **Jakob Mann**[2]

Abstract We develop a model that predicts all two-point correlations in high Reynolds number turbulent flow, in both space and time. This is accomplished by combining the design philosophies behind two existing models, the Mann spectral velocity tensor, in which isotropic turbulence is distorted according to rapid distortion theory, and Kristensen's longitudinal coherence model, in which eddies are simultaneously advected by larger eddies as well as decaying. The model is compared with data from both observations and large-eddy simulations and is found to predict spatial correlations comparable to the Mann spectral tensor and temporal coherence better than any known model. Within the developed framework, Lagrangian two-point correlations in space and time are also predicted, and the predictions are compared with measurements of isotropic turbulence. The required input to the models, which are formulated as spectral velocity tensors, can be estimated from measured spectra or be derived from the rate of dissipation of turbulent kinetic energy, the friction velocity and the mean shear of the flow. The developed models can, for example, be used in wind-turbine engineering, in applications such as lidar-assisted feed forward control and wind-turbine wake modelling.

Keywords Sheared turbulence · Spectral velocity tensor · Two-point correlations

1 Introduction

Renewed interest in the spatio-temporal structure of sheared turbulence comes from research in wind energy, and whether forward-looking light detection and ranging (lidar) systems can reduce mechanical loads on wind turbines by anticipating incoming gusts (Pao and Johnson

✉ Martin de Maré
  mardm@dongenergy.dk

[1] Wind Power, DONG Energy, Gentofte, Denmark

[2] Wind Energy Department, Risø Campus, Technical University of Denmark (DTU),
  Lyngby, Denmark

2011; Bossanyi et al. 2012; Mikkelsen et al. 2013). The potential for both extreme and fatigue load reduction seems obvious, but to model the complex interactions between lidar-sensed turbulence and wind-turbine control and aerodynamics it is necessary to have a realistic model for the spatio-temporal structure of turbulence (Bossanyi 2013).

Most turbine-mounted lidars are placed close to the centre of the rotor, either on the nacelle or in the spinner, the aerodynamically shaped cover of the wind turbine rotor hub. Fluctuations along the direction of the mean flow constitute the most important turbulence component of the loads on the rotor. However, if a lidar is to measure these fluctuations over a rotor sized area upwind of the turbine, it would for geometrical reasons have to measure quite far upstream. The question arises whether the turbulent fluctuations measured there would arrive unchanged to the rotor a short time later, or equivalently, whether departures from Taylor's frozen turbulence hypothesis are important. For a nacelle-mounted lidar Simley et al. (2014) found that measurements made approximately one rotor diameter upstream reproduce most faithfully the gusts that impinge on the rotor. If measured further upstream, decorrelation during the advection to the rotor starts to become important. If measured closer to the rotor, fluctuations in directions other than along the mean flow will contaminate the measurements. Related questions pertain to how many beam directions will cover the rotor in an optimal way (Schlipf et al. 2013), and how the significant probe volume of the lidar influences the measurements (Sathe and Mann 2013). All these issues depend on the spatial and temporal structure of sheared turbulence, the subject of the present study.

Wind-turbine wakes are important not only because they affect the energy production adversely for downwind turbines in a wind farm but also because they increase dynamic loads on rotors intersecting them. Dynamic loads arise mainly because the blades of a downwind turbine partly in the wake of another, go in and out of the region with the wake velocity deficit. Another important effect is that wakes can meander such that the entire rotor of a downwind turbine alternately experiences unaffected flow and the reduced flow velocity of the wake. This typically creates dynamic loads that are greater than those on a free-standing turbine. A popular way to model wake meandering assumes wakes to be advected passively in a frozen turbulence field (Larsen et al. 2008). A more realistic wake-meandering model may include the temporal evolution as well. Such a model would then likely require both the spatial and temporal structure of sheared turbulence as input.

Spatial correlations are tractable to describe in the Fourier domain by the use of a spectral velocity tensor (see e.g. Pope 2000). In Mann (1994), rapid distortion theory was employed to produce a spectral velocity tensor describing turbulence subjected to uniform shear. That model was recently tested over homogeneous terrain for different values of aerodynamic roughness length by Chougule et al. (2014) and for offshore conditions by de Maré and Mann (2014). Alternative rapid distortion formulations include a formulation with blocking effects from the ground also explored in Mann (1994), and formulations including buoyancy effects, investigated e.g by Hanazaki and Hunt (2004) and Chougule (2013). In Kristensen (1979), a model was developed to predict the correlation between two wind measurements separated in the streamwise direction. This model primarily predicts temporal correlations, and it has recently been implemented and used by Bossanyi (2013) in the context of lidar-assisted wind-turbine control.

In Sect. 2, after first introducing definitions, we attempt to combine the design philosophy of the Mann (1994) tensor, in which isotropic turbulence is distorted by uniform shear, with the design philosophy of Kristensen (1979), in which eddies are simultaneously advected randomly by larger eddies as well as decaying. In Sect. 3, we discuss the implementation of the developed model as well as strategies for obtaining the necessary input information. Finally in Sect. 4, we compare the predictions of our model to observations from experiments,

data from large-eddy simulation (LES) and, where applicable, to the predictions of the Mann (1994) tensor.

Saffman (1963), Hunt et al. (1987), and more recently Wilczek and Narita (2012) and Wilczek et al. (2014), suggested the temporal evolution of the velocity tensor to be given by wavenumber-dependent Gaussian functions. A number of such models were evaluated for isotropic turbulence in Ott and Mann (2005). As the validation section includes comparisons with those same experiments, comparisons with the models evaluated in Ott and Mann (2005) are implicitly made.

2 Modelling

2.1 Preliminaries

It is common to assume statistical stationarity (as well as ergodicity) and decompose the three-dimensional flow velocity, $\tilde{u}(x, t)$, into a mean velocity, $U(x)$, and a fluctuating part, $u(x, t)$. We define the coordinate system to move with a suitable velocity, U_0, so that in our coordinate system $U(0) = 0$. We further assume a constant and non-negative shear, $\mathrm{d}U_1/\mathrm{d}z$, such that

$$\tilde{u}(x, t) = U(x) + u(x, t) = \left(x_3 \frac{\mathrm{d}U_1}{\mathrm{d}z}, 0, 0\right) + u(x, t), \tag{1}$$

where z and x_3 are used interchangeably. Provided that $u(x, t)$ is statistically homogeneous, we can define a covariance tensor

$$R_{ij}(r, \tau) = \left\langle u_i(x, t)\, u_j(x + r + U(x + r)\tau, t + \tau)\right\rangle. \tag{2}$$

In (2) we have accounted for the mean velocity of the flow varying with height by introducing the term $U(x + r)\tau$, thereby modifying the traditional definition of the covariance tensor. The role of this term is easiest to demonstrate for $r = 0$, when it causes the right-hand side of (2) to denote the covariance at a point that moves with the mean flow velocity, $U(x)$. The spectral velocity tensor (or velocity-spectrum tensor), $\widehat{R}_{ij}$, is the spatial Fourier transform of (2),

$$\widehat{R}_{ij}(k, \tau) = \frac{1}{(2\pi)^3} \iiint R_{ij}(r, \tau)\, \mathrm{e}^{-\mathrm{i} k \cdot r}\, \mathrm{d}^3 r, \tag{3}$$

where $\mathrm{d}^3 r = \mathrm{d}r_1\, \mathrm{d}r_2\, \mathrm{d}r_3$. From the spectral velocity tensor a number of quantities can be derived, for example the (one-dimensional) spatial cross-spectrum

$$\chi_{ij}(k_1, r, \tau) = \frac{1}{2\pi} \int R_{ij}((\xi_1, 0, 0) + r, \tau)\, \mathrm{e}^{-\mathrm{i} k_1 \xi_1}\, \mathrm{d}\xi_1$$
$$= \iint_{\kappa_1 = k_1} \widehat{R}_{ij}(\kappa, \tau)\, \mathrm{e}^{\mathrm{i}\kappa \cdot r}\, \mathrm{d}^2 \kappa, \tag{4}$$

and the closely related quantity

$$\mathring{\chi}_{ij}(k) = \iint_{|\kappa| = k} \widehat{R}_{ij}(\kappa, 0)\, \mathrm{d}^2 \kappa. \tag{5}$$

From the spatial cross-spectra the spatial spectral coherence is in turn derived as

$$\mathrm{coh}_{ij}(k_1, r, \tau) = \frac{|\chi_{ij}(k_1, r, \tau)|^2}{\chi_{ii}(k_1, r, 0)\, \chi_{jj}(k_1, r, 0)}, \tag{6}$$

where, as our only exception, no summation over repeated indices is intended.

Batchelor (1953) used a generalized stochastic Fourier–Stieltjes decomposition of the fluctuating part of the wind velocity; however, as we find this notation somewhat unintuitive we use the less stringent notation

$$u(x, t) = \iiint \widehat{u}(k, t) \, e^{i k \cdot x} \, d^3 k. \tag{7}$$

We find that

$$
\begin{aligned}
u\left(\left(x_1 + x_3 \frac{dU_1}{dz} \tau, x_2, x_3 \right), t + \tau \right) \\
= \iiint \widehat{u}(\kappa, t + \tau) \, e^{i \kappa \cdot \left(x_1 + x_3 \frac{dU_1}{dz} \tau, x_2, x_3 \right)} \, d^3 \kappa \\
= \iiint \widehat{u}\left(\left(k_1, k_2, k_3 - \frac{dU_1}{dz} \tau \, k_1 \right), t + \tau \right) e^{i k \cdot x} \, d^3 k,
\end{aligned} \tag{8}
$$

where in the last step the variable transformation

$$\kappa = (\kappa_1, \kappa_2, \kappa_3) = \left(k_1, k_2, k_3 - \frac{dU_1}{dz} \tau \, k_1 \right) \tag{9}$$

has been used. Combining (8) with (2) and (3) it is possible to show that

$$\widehat{R}_{ij}(k, \tau) = \left\langle \widehat{u}_i(k, t) \overline{\widehat{u}_j(k(\tau), t + \tau)} \, d^3 k \right\rangle, \tag{10}$$

where we have introduced notation for complex conjugation, and $k(\tau)$ has been introduced as

$$k(\tau) = \left(k_1, k_2, k_3 - \frac{dU_1}{dz} \tau \, k_1 \right). \tag{11}$$

Formulating a model for $\widehat{R}_{ij}(k, \tau)$ is one of our goals. For comparison, Mann (1994) developed a model for $\widehat{R}_{ij}(k, 0)$ and Kristensen (1979) developed a model for $\mathrm{coh}_{11}(k_1, 0, \tau)$. We are also interested in the Lagrangian covariance tensor defined by

$$R_{ij}^{\mathrm{L}}(r, \tau) = \left\langle u_i(x, t_0) \, u_j\left(X_{t_0}^{\mathrm{L}}(x + r, t_0 + \tau), t_0 + \tau \right) \right\rangle, \tag{12}$$

where $X_{t_0}^{\mathrm{L}}(x, t)$ is the position at time t of a fluid particle, which at t_0 was located at x. Therefore we also attempt to model the Lagrangian spectral velocity tensor defined through

$$\widehat{R}_{ij}^{\mathrm{L}}(k, \tau) = \frac{1}{(2\pi)^3} \iiint R_{ij}^{\mathrm{L}}(r, \tau) \, e^{-i k \cdot r} \, d^3 r. \tag{13}$$

We will frequently sacrifice physical realism for mathematical tractability. One such example is our assumption of constant shear, which in reality would create infinitely large turbulent eddies. This particular problem is handled by having a turbulent length scale as a model input. Due to such simplifications, in the end, it will be the prediction capabilities of the final models that determine their applicability.

2.2 Analysis of Eddy Decay

The focus here is the evolution of turbulent eddies in the presence of vertical shear, excluding the turbulent advection of small-scale eddies by larger eddies, a topic we address instead
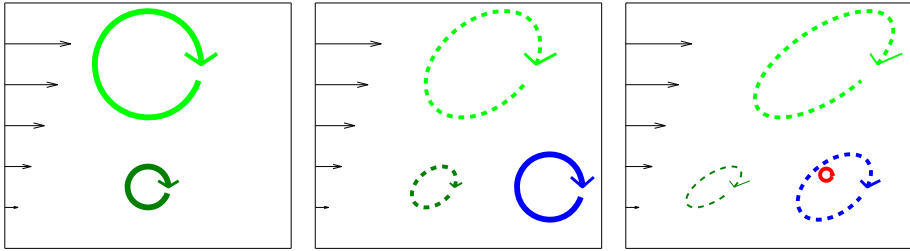
Fig. 1 The three frames show a sequence of snapshots of conceptual turbulence distorted by shear (illustrated by the *black arrows*). The two *green* eddies are distorted (from *circles* to *ellipses*) by the shear while at the same time decaying (illustrated by the shift from *solid lines* to *dashed lines*). We note that the smaller, *dark green*, eddy appears to decay more rapidly than the larger, *light green*, eddy. We also note the newborn *blue* and *red* eddies in the middle and right-most frames, respectively

in the next section. We start from the rapid distortion equation for sheared flow derived by Moffatt (1967) and Townsend (1976),

$$\frac{D \widehat{u}_i(\boldsymbol{k}(t), t)}{D t} = \frac{dU_1}{dz} \left(-\delta_{i1} + 2 \frac{k_i k_1}{|\boldsymbol{k}(t)|^2} \right) \widehat{u}_3(\boldsymbol{k}(t), t), \tag{14}$$

where

$$\boldsymbol{k}(t) = \left(k_1, k_2, k_{30} - k_1 \frac{dU_1}{dz} (t - t_0) \right). \tag{15}$$

Equation 14 does not include any term for buoyancy effects, so the results may or may not be valid for non-neutral atmospheric stratification. More elaborate rapid distortion formulations are in use (Kaneda and Ishida 2000; Hanazaki and Hunt 2004; Salhi and Cambon 2010; Chougule 2013); however, we stay with the above version for now.

In Fig. 1 we show a sequence of snapshots of conceptual turbulence; the sequence of snapshots is continued in Fig. 2, in which the dashed black lines illustrate the distortion of a sample wavenumber according to (15). We now write $\widehat{\boldsymbol{u}}(\boldsymbol{k}, t)$ as

$$\widehat{\boldsymbol{u}}(\boldsymbol{k}, t) = \int_{-\infty}^{t} \boldsymbol{\eta}(\boldsymbol{k}_0, t_0, t - t_0) \, dt_0, \tag{16}$$

where we have introduced $\boldsymbol{\eta}(\boldsymbol{k}_0, t_0, t - t_0) \, dt_0$ as the contribution to $\widehat{\boldsymbol{u}}(\boldsymbol{k}, t)$ from eddies that were created between t_0 and $t_0 + dt_0$. The newborn eddies in Fig. 1 would thus contribute to different $\boldsymbol{\eta}$ than the older eddies in the same frames. In (16) $\boldsymbol{k}_0$ is derived from $\boldsymbol{k}$ by inverting (15),
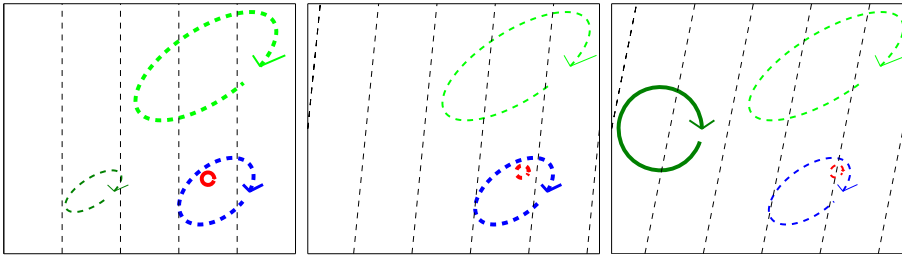
$$\boldsymbol{k}_0 = (k_1, k_2, k_{30}) = \left(k_1, k_2, k_3 + k_1 \frac{dU_1}{dz} (t - t_0) \right). \tag{17}$$

It follows from homogeneity that for a fixed t, the $\boldsymbol{\eta}$'s contributing to *different* wavenumbers are uncorrelated. We, however, go beyond homogeneity and postulate that

$$\left\langle \eta_i(\boldsymbol{k}_0, t_0, t - t_0) \overline{\eta_j(\boldsymbol{\kappa}_0, \tau_0, t - \tau_0 + \tau)} \, d^3\boldsymbol{k} \, dt_0 \right\rangle = 0 \tag{18}$$

unless $\tau_0 = t_0$ and $\boldsymbol{\kappa}_0 = \boldsymbol{k}_0$. This assumption reduces our objective of determining $\widehat{R}_{ij}$, to quantifying

$$\left\langle \eta_i(\boldsymbol{k}_0, t_0, t - t_0) \overline{\eta_j(\boldsymbol{k}_0, t_0, t - t_0 + \tau)} \, d^3\boldsymbol{k} \, dt_0 \right\rangle, \tag{19}$$

Fig. 2 The three frames are a continuation of the sequence of conceptual turbulence in Fig. 1. The *left-most* frame is identical to the last frame of Fig. 1, except that the shear is now illustrated by the *dashed black lines* which represent a wavenumber evolving according to $\mathbf{k}(\tau) = \left(k_1, k_2, k_3 - \frac{\mathrm{d}U_1}{\mathrm{d}z} \tau\, k_1\right)$. In the two *right-most* frames we notice that the *blue* eddy advects the smaller red eddy, causing it to move relative to the illustrated wavenumber

as we can then use (10) and (16) to find $\widehat{R}_{ij}$. Direct validation of (18) would require isolating the contribution of newly formed eddies, from the contributions of older eddies, an objective that may be challenging, to say the least, in practice.

We introduce the expected contribution from newborn eddies,

$$N_{ij}(\mathbf{k}_0) = \left\langle \eta_i(\mathbf{k}_0, t_0, 0)\overline{\eta_j(\mathbf{k}_0, t_0, 0)}\, \mathrm{d}^3\mathbf{k}\, \mathrm{d}t_0 \right\rangle, \tag{20}$$

which is constant in time due to stationarity. As the eddies are expected to decay over time the contributions cannot, however, be expected to be statistically stationary with respect to $t - t_0$.

Townsend (1976) suggested that the time evolution of an eddy can be described as a superposition of rapid distortion and viscous decay. Inspired by this argument and Mann (1994) we introduce into the rapid distortion equation a term where the eddy viscosity depends on $\mathbf{k}(t)$. Continuing to disregard advection by larger eddies, we thus postulate that the contributions, $\boldsymbol{\eta}$, evolve in time according to the deterministic equation,

$$\frac{\mathrm{D}\,\eta_i(\mathbf{k}_0, t_0, t - t_0)}{\mathrm{D}\,t} = \frac{\mathrm{d}U_1}{\mathrm{d}z}\left(-\delta_{i1} + 2\frac{k_i k_1}{|\mathbf{k}(t)|^2}\right)\eta_3(\mathbf{k}_0, t_0, t - t_0)$$
$$- \frac{1}{2\,\tau_e(\mathbf{k}(t))}\eta_i(\mathbf{k}_0, t_0, t - t_0), \tag{21}$$

where the eddy viscosity term is the last term on the right-hand side. We refer to the process described by (21) as eddy decay.

For the isotropic case, where $\mathrm{d}U_1/\mathrm{d}z = 0$ and therefore $\mathbf{k}(t) = \mathbf{k}_0$, the solution to (21) is simply

$$\boldsymbol{\eta}^{\mathrm{ISO}}(\mathbf{k}_0, t_0, t - t_0) = \boldsymbol{\eta}_{t_0}^{\mathrm{ISO}}(\mathbf{k}_0, t_0, 0)\exp\left(-\frac{t - t_0}{2\,\tau_e(\mathbf{k}_0)}\right). \tag{22}$$

From this solution it can be seen that the expected lifetime of the energy of eddies created at the same time is

$$\frac{\int_{t=t_0}^{\infty} \boldsymbol{\eta}^{\mathrm{ISO}}(\mathbf{k}_0, t_0, t - t_0) \cdot \overline{\boldsymbol{\eta}^{\mathrm{ISO}}(\mathbf{k}_0, t_0, t - t_0)}\, \mathrm{d}t}{\boldsymbol{\eta}^{\mathrm{ISO}}(\mathbf{k}_0, t_0, 0) \cdot \overline{\boldsymbol{\eta}^{\mathrm{ISO}}(\mathbf{k}_0, t_0, 0)}}$$
$$= \int_{t=t_0}^{\infty} \exp\left(-\frac{t - t_0}{2\,\tau_e(\mathbf{k})}\right)\exp\left(-\frac{t - t_0}{2\,\tau_e(\mathbf{k})}\,\mathrm{d}t\right)$$
$$= \tau_e(\mathbf{k}). \tag{23}$$

Based on (23) we refer to $\tau_e(\boldsymbol{k})$ as the eddy lifetime, even though this is not an entirely accurate term when $\mathrm{d}U_1/\mathrm{d}z \neq 0$. In Fig. 1 we have illustrated the dependence of τ_e on $\boldsymbol{k}$ by the smaller eddies decaying more rapidly than the large ones.

The general solution to (21) can be written

$$\boldsymbol{\eta}(\boldsymbol{k}_0, t_0, t - t_0) = \boldsymbol{B}(\boldsymbol{k}_0, t - t_0)\, \boldsymbol{\eta}(\boldsymbol{k}_0, t_0, 0), \tag{24}$$

where

$$\boldsymbol{B}(\boldsymbol{k}_0, t - t_0) = \exp\left(-\left(\Omega(\boldsymbol{k}_0, t - t_0) - \Omega(\boldsymbol{k}_0, 0)\right)\right) \begin{bmatrix} 1 & 0 & \zeta_1\left(\boldsymbol{k}_0, \frac{\mathrm{d}U_1}{\mathrm{d}z}(t - t_0)\right) \\ 0 & 1 & \zeta_2\left(\boldsymbol{k}_0, \frac{\mathrm{d}U_1}{\mathrm{d}z}(t - t_0)\right) \\ 0 & 0 & |\boldsymbol{k}_0|^2/|\boldsymbol{k}(t)|^2 \end{bmatrix}, \tag{25}$$

and where in turn $\zeta_1(\boldsymbol{k}_0, \beta)$ and $\zeta_2(\boldsymbol{k}_0, \beta)$, derived in Mann (1994) and Townsend (1976), are

$$
\begin{aligned}
\zeta_1(\boldsymbol{k}_0, \beta) = {} & \frac{\beta k_1^2 \left(|\boldsymbol{k}_0|^2 - 2k_{30}^2 + \beta k_1 k_{30}\right)}{|\boldsymbol{k}(t)|^2 \left(k_1^2 + k_2^2\right)} \\
& - \frac{k_2^2 |\boldsymbol{k}_0|^2}{k_1 \left(k_1^2 + k_2^2\right)^{3/2}} \arctan\left(\frac{\beta k_1 \left(k_1^2 + k_2^2\right)^{1/2}}{|\boldsymbol{k}_0|^2 - \beta k_1 k_{30}}\right),
\end{aligned}
\tag{26}
$$

$$
\begin{aligned}
\zeta_2(\boldsymbol{k}_0, \beta) = {} & \frac{k_2 \beta k_1 \left(|\boldsymbol{k}_0|^2 - 2k_{30}^2 + \beta k_1 k_{30}\right)}{|\boldsymbol{k}(t)|^2 \left(k_1^2 + k_2^2\right)} \\
& + \frac{k_2 |\boldsymbol{k}_0|^2}{\left(k_1^2 + k_2^2\right)^{3/2}} \arctan\left(\frac{\beta k_1 \left(k_1^2 + k_2^2\right)^{1/2}}{|\boldsymbol{k}_0|^2 - \beta k_1 k_{30}}\right),
\end{aligned}
\tag{27}
$$

and $\Omega(\boldsymbol{k}_0, t - t_0)$ has been introduced such that

$$\frac{\partial \Omega(\boldsymbol{k}_0, t - t_0)}{\partial t} = \frac{1}{2\, \tau_e(\boldsymbol{k}(t))}. \tag{28}$$

For comparison, in Mann (1994) the eddies are not continuously decaying. Instead the eddy lifetime, $\tau_e(\boldsymbol{k})$, is used as the typical time the eddies contributing to $\boldsymbol{k}$ have been subjected to the rapid distortion.

We end by noting that eddy decay can be applied sequentially, i.e that

$$B_{im}(\boldsymbol{k}(t), \tau)\, B_{mj}(\boldsymbol{k}_0, t - t_0) = B_{ij}(\boldsymbol{k}_0, t - t_0 + \tau). \tag{29}$$

2.3 Modelling Advection by Larger Eddies

Kristensen (1979) attributed the loss of longitudinal coherence to a combination of eddies decaying, and large eddies advecting smaller eddies, causing them to miss the downstream anemometer. The latter process, which is not captured by rapid distortion theory, is illustrated in Fig. 2. A straightforward way of modelling this advection by larger eddies is to assume that an eddy moves as a suitably sized sphere. To be more exact, let us assume that an eddy with a size corresponding to wavenumber of magnitude k, positioned at $\boldsymbol{x}$ at time t, has a velocity $u_i^{R_k}(\boldsymbol{x}, t)$, which is the average velocity over a sphere with radius R_k, i.e.,

$$u_i^{R_k}(\boldsymbol{x}, t) = \frac{\iiint_{|\boldsymbol{r}| < R_k} u_i(\boldsymbol{x} + \boldsymbol{r}, t)\, \mathrm{d}^3 \boldsymbol{r}}{\frac{4}{3}\pi R_k^3}. \tag{30}$$

Assuming that eddies move like spheres may not be entirely realistic because a sphere has a well-defined edge whereas an eddy most likely does not. It can also be argued that owing to eddy decay the shape of a typical eddy would be better represented by an ellipsoid, rather than by a sphere.

Inspired by (3), if we were to define a spectral velocity tensor based on the averaged wind velocity of (30) we would, for $\tau = 0$, obtain

$$\widehat{R}_{ij}^{R_k}(\boldsymbol{\kappa}, 0) = \mathrm{H}_k^2(|\boldsymbol{\kappa}|)\widehat{R}_{ij}(\boldsymbol{\kappa}, 0), \tag{31}$$

where

$$\mathrm{H}_k(\kappa) = -3\frac{\kappa R_k \cos(\kappa R_k) - \sin(\kappa R_k)}{\kappa^3 R_k^3} \tag{32}$$

is the Fourier transform of the "averaging sphere" convolution kernel, which, we may add, effectively acts as a low-pass filter. The right-hand side of (32) is a scaled version of the Bessel function $J_{3/2}(x)$. Based on the argument that eddies do not advect themselves, we select R_k such that kR_k equals the first zero of $J_{3/2}(x)$, i.e.

$$R_k \approx \frac{4.4934}{k}. \tag{33}$$

We note that $R_k = \pi/k$ or $R_k = \pi/2k$ would be just as natural a choice as (33). We will briefly return to this topic when discussing the cross-over point of Eulerian and Lagrangian covariances in Sect. 4.2.

From $\widehat{R}_{ij}^{R_k}(\boldsymbol{\kappa}, 0)$ in (31) we can, among many other quantities, derive the standard deviation of $u_i^{R_k}(\boldsymbol{x}, t)$ along any vector. We take the opportunity to introduce, $s(\boldsymbol{k})$, the standard deviation of the velocity of the eddies with radius $R_{|\boldsymbol{k}|}$, in the direction of $\boldsymbol{k}$,

$$s(\boldsymbol{k}) = \sqrt{\left\langle \left| \frac{k_i k_j}{|\boldsymbol{k}|^2} u_i^{R_{|\boldsymbol{k}|}}(\boldsymbol{x}, t) u_j^{R_{|\boldsymbol{k}|}}(\boldsymbol{x}, t) \right\rangle \right.} = \sqrt{\iiint \frac{k_i k_j}{|\boldsymbol{k}|^2} \mathrm{H}_{|\boldsymbol{k}|}^2(|\boldsymbol{\kappa}|)\widehat{R}_{ij}(\boldsymbol{\kappa}, 0)\, \mathrm{d}^3\boldsymbol{\kappa}}$$

$$= \sqrt{\int_0^\infty \frac{k_i k_j}{|\boldsymbol{k}|^2} \mathrm{H}_{|\boldsymbol{k}|}^2(\kappa)\mathring{\chi}_{ij}(\kappa)\, \mathrm{d}\kappa}. \tag{34}$$

Now, let us again consider the blue eddy in Fig. 2. If we denote the illustrated wavenumber $\boldsymbol{k}(t)$ and assume that $R_{|\boldsymbol{k}|}$ happens to be the characteristic size of the blue eddy, then, according our definitions, the blue eddy moves with a velocity

$$v_{\mathrm{blue}}(t) = \frac{k_i}{|\boldsymbol{k}(t)|} u_i^{R_{|\boldsymbol{k}|}}(\boldsymbol{x}_{\mathrm{blue}}(t), t), \tag{35}$$

in the direction of $\boldsymbol{k}(t)$, i.e. perpendicular to the dashed black lines. If the blue eddy is the only eddy described by $\boldsymbol{\eta}(\boldsymbol{k}_0, t_0, t - t_0)$, then $\boldsymbol{\eta}(\boldsymbol{k}_0, t_0, t - t_0 + \tau)$ is equal to

$$\boldsymbol{B}(\boldsymbol{k}, \tau)\boldsymbol{\eta}(\boldsymbol{k}_0, t_0, t - t_0)\, \mathrm{e}^{-\mathrm{i}\,\phi_{\mathrm{blue}}(\tau)}, \tag{36}$$

with $\phi_{\mathrm{blue}}(\tau)$ the "distance travelled in radians" given by

$$\phi_{\mathrm{blue}}(\tau) = \int_t^{t+\tau} v_{\mathrm{blue}}(\tau')|\boldsymbol{k}(\tau')|\, \mathrm{d}\tau'. \tag{37}$$

Now, $\boldsymbol{\eta}(\boldsymbol{k}_0, t_0, t - t_0)$ not only represents the blue eddy, but all eddies of approximately the same size and age as the blue eddy. Equation 34 introduced the standard deviation of the velocity of these eddies in the direction of $\boldsymbol{k}$, as $s(\boldsymbol{k})$, and we assume that $s(\boldsymbol{k})$, analogously

to (37), can be integrated to give the standard deviation of the distance in radians travelled by the eddies,

$$\Theta(\boldsymbol{k}, \tau) = \int_t^{t+\tau} s\big(\boldsymbol{k}(\tau')\big) |\boldsymbol{k}(\tau')| \, \mathrm{d}\tau'. \tag{38}$$

We further assume that the distances in radians travelled by the eddies in question are normally distributed,

$$\frac{1}{\Theta(\boldsymbol{k}, \tau)\sqrt{2\pi}} \exp\left(-\frac{\phi^2}{2\Theta^2(\boldsymbol{k}, \tau)}\right), \tag{39}$$

a choice supported by the fact that this distribution has maximal entropy for given first and second moments. Combining (36) with (39) leads to

$$
\begin{aligned}
&\left\langle \eta_i(\boldsymbol{k}_0, t_0, t - t_0)\overline{\eta_j(\boldsymbol{k}_0, t_0, t - t_0 + \tau)} \, \mathrm{d}^3\boldsymbol{k} \, \mathrm{d}t_0 \right\rangle \\
&= \left\langle \eta_i(\boldsymbol{k}_0, t_0, t - t_0)\overline{\left(\int_{-\infty}^{\infty} \frac{1}{\Theta(\boldsymbol{k}, \tau)\sqrt{2\pi}} \, \mathrm{e}^{-\frac{\phi^2}{2\Theta^2(\boldsymbol{k}, \tau)}} \, B_{jn}(\boldsymbol{k}, \tau)}\right.\right. \\
&\qquad \overline{\left.\eta_j(\boldsymbol{k}_0, t_0, t - t_0 + \tau)\, \mathrm{e}^{-i\phi(\tau)} \, \mathrm{d}\phi\right)} \, \mathrm{d}^3\boldsymbol{k} \, \mathrm{d}t_0 \Bigg\rangle \\
&= \left\langle \eta_m(\boldsymbol{k}_0, t_0, t - t_0)\overline{\mathrm{e}^{-\frac{1}{2}\Theta^2(\boldsymbol{k}, \tau)} \, B_{jn}(\boldsymbol{k}, \tau)\eta_n(\boldsymbol{k}_0, t_0, t - t_0)} \, \mathrm{d}^3\boldsymbol{k} \, \mathrm{d}t_0 \right\rangle \\
&= \mathrm{e}^{-\frac{1}{2}\Theta^2(\boldsymbol{k}, \tau)} \, B_{im}(\boldsymbol{k}_0, t - t_0) N_{mn}(\boldsymbol{k}_0) B_{jn}(\boldsymbol{k}_0, t + \tau - t_0), \tag{40}
\end{aligned}
$$

where in the last step we have used (20) and (29). The last line of (40) describes newborn eddies, $N_{mn}(\boldsymbol{k}_0)$, swhich, since their birth at t_0, have been subjected to eddy decay, $B_{ij}(\boldsymbol{k}_0, t - t_0)$. Moreover, if observed twice, at t and $t + \tau$, advection by larger eddies has caused unalignment resulting in a loss of correlation according to $\exp\left(-\frac{1}{2}\Theta^2(\boldsymbol{k}, \tau)\right)$.

We can now, using (10), (16), (18) and (40), derive an expression for $\widehat{R}_{ij}(\boldsymbol{k}, \tau)$,

$$
\begin{aligned}
\widehat{R}_{ij}(\boldsymbol{k}, \tau) &= \left\langle \widehat{u}_i(\boldsymbol{k}, t)\overline{\widehat{u}_j(\boldsymbol{k}(\tau), t + \tau)} \, \mathrm{d}^3\boldsymbol{k} \right\rangle \\
&= \left\langle \int_{-\infty}^t \eta_i(\boldsymbol{k}, \xi_0, t - \xi_0) \, \mathrm{d}\xi_0 \int_{-\infty}^t \overline{\eta_j(\boldsymbol{k}_\tau, \zeta_0, t - \zeta_0)} \, \mathrm{d}\zeta_0 \, \mathrm{d}^3\boldsymbol{k} \right\rangle \\
&= \int_{-\infty}^t \left\langle \eta_i(\boldsymbol{k}_0, t_0, t - t_0)\overline{\eta_j(\boldsymbol{k}_0, t_0, t + \tau - t_0)} \, \mathrm{d}^3\boldsymbol{k} \, \mathrm{d}t_0 \right\rangle \mathrm{d}t_0 \\
&= \int_{-\infty}^t \mathrm{e}^{-\frac{1}{2}\Theta^2(\boldsymbol{k}, \tau)} \, B_{im}(\boldsymbol{k}_0, t - t_0) N_{mn}(\boldsymbol{k}_0) B_{jn}(\boldsymbol{k}_0, t + \tau - t_0) \, \mathrm{d}t_0, \quad (41)
\end{aligned}
$$

where $\boldsymbol{k}_0$ and and $\Theta(\boldsymbol{k}, \tau)$ are given by (17) and (38), respectively. We note that $\Theta(\boldsymbol{k}, \tau)$ by definition $= 0$ for $\tau = 0$ and it is therefore not a problem that $\widehat{R}_{ij}(\boldsymbol{k}, 0)$ is used, through the definition of $s(\boldsymbol{k})$, to define $\Theta(\boldsymbol{k}, \tau)$. Owing to stationarity, the right-hand side of (41) does not depend on the value of t.

We cannot evaluate (41) numerically just yet because we have neither introduced an expression for the eddy lifetime nor an expression for the added energy due to newborn eddies, $N_{ij}(\boldsymbol{k}_0)$. Before addressing these needs, we turn our attention to the Lagrangian covariance tensor, $\widehat{R}_{ij}^{\mathrm{L}}$, defined in (13).

2.4 A Model for the Lagrangian Tensor

The Lagrangian approach can be described as observing the flow by tracking fluid particles and recording their instantaneous velocities. If we follow one of the fluid particles within the small red eddy of Fig. 2 and use it to study the wavenumber illustrated by the dashed black lines, then it is clear that the Lagrangian velocity may lose coherence even when, as in this case, the blue eddy (which likely contributes to the illustrated wavenumber) stays more or less coherent. Our assumption is therefore that the evolution of the Lagrangian tensor is a combination of eddy decay and the fluid particles moving relative to the eddies of which they are a part.

If we want to quantify the movement of a point within the small red eddy, relative to the red eddy itself, then the fact that the blue eddy is advecting both the red eddy and our observation particle should be of little importance. Similarly, if we are interested in the point's movement relative to the blue eddy, then the fact that it is also moving within the small red eddy likely has limited impact. Based on these arguments we quantify the velocity of a particle relative to an eddy of size $R_{|\boldsymbol{k}|}$, as the velocity of the particle minus both the velocity contribution from eddies that are large enough to move the eddy of interest, $H_{|\boldsymbol{k}|}(|\boldsymbol{\kappa}|)\widehat{u}_i(\boldsymbol{\kappa}, 0)$, and the velocity contribution from eddies that are small enough to be moved by the eddy of interest, $H_{|\boldsymbol{\kappa}|}(|\boldsymbol{k}|)\widehat{u}_i(\boldsymbol{\kappa}, 0)$. The standard deviation of the velocity with which a fluid particle moves relative to its eddy in the direction of $\boldsymbol{k}$ can then be quantified as

$$
\begin{aligned}
s_{\mathrm{L}}(\boldsymbol{k}) &= \sqrt{\iiint \frac{k_i k_j}{|\boldsymbol{k}|^2}\left(1 - H_{|\boldsymbol{k}|}(|\boldsymbol{\kappa}|) - H_{|\boldsymbol{\kappa}|}(|\boldsymbol{k}|)\right)^2 \widehat{R}_{ij}(\boldsymbol{\kappa}, 0)\,\mathrm{d}^3\boldsymbol{\kappa}} \\
&= \sqrt{\int_0^\infty \frac{k_i k_j}{|\boldsymbol{k}|^2}\left(1 - H_{|\boldsymbol{k}|}(|\boldsymbol{\kappa}|) - H_{|\boldsymbol{\kappa}|}(|\boldsymbol{k}|)\right)^2 \mathring{\chi}_{ij}(\kappa)\,\mathrm{d}\kappa}.
\end{aligned}
\tag{42}
$$

The factor $\left(1 - H_{|\boldsymbol{k}|}(|\boldsymbol{\kappa}|) - H_{|\boldsymbol{\kappa}|}(|\boldsymbol{k}|)\right)^2$ is illustrated for $|\boldsymbol{k}| = 1$ in Fig. 3.
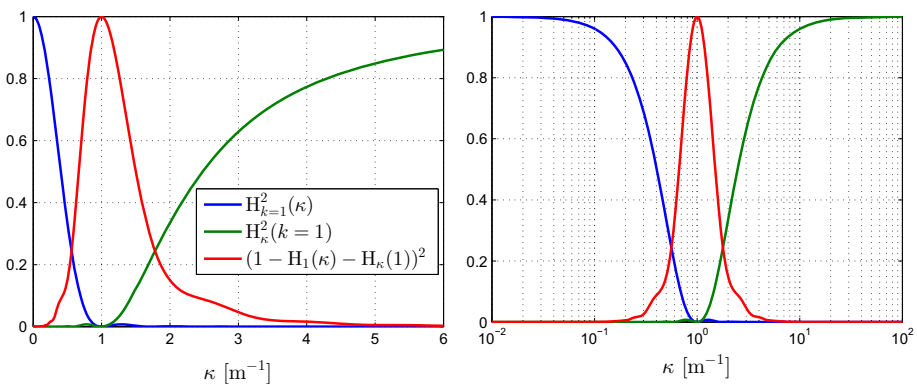
Fig. 3 The velocity of a particle relative to an eddy of size $R_{|\boldsymbol{k}|=1}$ is quantified as the velocity of the particle minus both the velocity contribution from eddies that are large enough to move the eddy of interest, $H_{|\boldsymbol{k}|=1}(|\boldsymbol{\kappa}|)\widehat{u}_i(\boldsymbol{\kappa}, 0)$, and the velocity contribution from eddies that are small enough to be moved by the eddy of interest, $H_{|\boldsymbol{\kappa}|}(|\boldsymbol{k}| = 1)\widehat{u}_i(\boldsymbol{\kappa}, 0)$. The resulting factor $(1 - H_1(\kappa) - H_\kappa(1))^2$ is illustrated (in *red*) versus a linear as well as a logarithmic κ. We note that the choice of expression for R_k in (33) ensures that $H_1(\kappa) = 0$ for $\kappa = 1$

Using similar arguments as the ones leading from (38) to (40) we arrive at modelling $\widehat{R}_{ij}^{\mathrm{L}}(\boldsymbol{k}, \tau)$ as

$$\widehat{R}_{ij}^{\mathrm{L}}(\boldsymbol{k}, \tau) = \int_{-\infty}^{t} \mathrm{e}^{-\frac{1}{2}\Theta_{\mathrm{L}}^2(\boldsymbol{k}, \tau)} B_{im}(\boldsymbol{k}_0, t - t_0) N_{mn}(\boldsymbol{k}_0) B_{jn}(\boldsymbol{k}_0, t + \tau - t_0) \, \mathrm{d}t_0, \qquad (43)$$

where $\boldsymbol{k}_0$ is given by (17), however, contrary to the Eulerian expression in (38), $\Theta_{\mathrm{L}}(\boldsymbol{k}, \tau)$ is now given by

$$\Theta_{\mathrm{L}}(\boldsymbol{k}, \tau) = \int_0^{\tau} s_{\mathrm{L}}(\boldsymbol{k}_{\tau'}) \, |\boldsymbol{k}(\tau')| \, \mathrm{d}\tau', \qquad (44)$$

where $\boldsymbol{k}(\tau') = \left(k_1, k_2, k_3 - \frac{\mathrm{d}U_1}{\mathrm{d}z}\tau' k_1\right)$ and $s_{\mathrm{L}}(\boldsymbol{k})$ is given by (42).

In terms of studying turbulence by tracking fluid particles and recording their instantaneous velocities, the right-hand side of (43) is the sum of the energy from newborn eddies, $N_{mn}(\boldsymbol{k}_0)$, that have been subjected to eddy decay, $B_{ij}(\boldsymbol{k}_0, t - t_0)$ since their birth at t_0. When attempting to make the observation, however, the tracked particles used for the observation have left their original positions relative to their designated eddy, and, therefore, lost correlation according to $\exp\left(-\frac{1}{2}\Theta_{\mathrm{L}}^2(\boldsymbol{k}, \tau)\right)$.

2.5 Remaining Modelling Choices

In order to evaluate (41) and (43) numerically we need expressions both for the added energy due to newborn eddies, $N_{ij}(\boldsymbol{k}_0)$, and for the eddy lifetime, $\tau_e(\boldsymbol{k})$. With the first objective in mind, we follow Kolmogorov (1968) and assume that the isotropic energy spectrum, $E(|\boldsymbol{k}|)$, which is closely related to the isotropic spectral velocity tensor, is only a function of $|\boldsymbol{k}|$ and the rate of dissipation of turbulent kinetic energy, ϵ, in the inertial subrange. Dimensional analysis then leads to

$$E(|\boldsymbol{k}|) \propto |\boldsymbol{k}|^{-\frac{5}{3}} \epsilon^{2/3}. \qquad (45)$$

An isotropic energy spectrum with this property was suggested by von Kármán (1948) as

$$E\left(\alpha_{\mathrm{K}}\epsilon^{2/3}, L_M, |\boldsymbol{k}|\right) = \alpha_{\mathrm{K}}\epsilon^{2/3} \frac{|\boldsymbol{k}|^4}{\left(L_M^{-1} + |\boldsymbol{k}|^2\right)^{17/6}}, \qquad (46)$$

where α_{K} is the Kolmogorov constant. With (46) we can write the isotropic spectral velocity tensor as

$$\widehat{R}_{ij}^{\mathrm{ISO}}\left(\alpha_{\mathrm{K}}\epsilon^{2/3}, L_M, \boldsymbol{k}\right) = \frac{E\left(\alpha_{\mathrm{K}}\epsilon^{2/3}, L_M, |\boldsymbol{k}|\right)}{4\pi |\boldsymbol{k}|^2} \left(\frac{\delta_{ij}|\boldsymbol{k}|^2 - k_i k_j}{|\boldsymbol{k}|^2}\right). \qquad (47)$$

Now, if we attempt to evaluate (41), for $\mathrm{d}U_1/\mathrm{d}z = 0$ and $\tau = 0$, using (23) we obtain

$$\widehat{R}_{ij}^{\mathrm{ISO}}(\boldsymbol{k}_0, 0) = \int_{-\infty}^{t} \left\langle \eta_i(\boldsymbol{k}_0, t_0, t - t_0)\overline{\eta_j(\boldsymbol{k}_0, t_0, t - t_0)} \, \mathrm{d}^3\boldsymbol{k} \, \mathrm{d}t_0 \right\rangle \mathrm{d}t_0$$

$$= \int_{-\infty}^{t} \mathrm{e}^{-\frac{t-t_0}{\tau_e(k)}} \left\langle \eta_i(\boldsymbol{k}_0, t_0, 0)\overline{\eta_j(\boldsymbol{k}_0, t_0, 0)} \, \mathrm{d}^3\boldsymbol{k} \, \mathrm{d}t_0 \right\rangle \mathrm{d}t_0 = \tau_e(\boldsymbol{k}_0)N_{ij}(\boldsymbol{k}_0).$$

$$(48)$$

Thus we have, for the isotropic case, quantified the added energy due to newborn eddies as

$$N_{ij}(\boldsymbol{k}_0) = \frac{\widehat{R}_{ij}^{\mathrm{ISO}}(\boldsymbol{k}_0)}{\tau_e(\boldsymbol{k}_0)}, \qquad (49)$$

and we will assume that (49) is approximately true also for the non-isotropic case. Equation 49 thus follows Mann (1994) in that the eddies start out isotropic and become anisotropic through rapid distortion.

Regarding the eddy lifetime, we can argue that, in the inertial subrange, $\tau_e(\boldsymbol{k})$ should only be a function of $|\boldsymbol{k}|$ and the rate of dissipation of turbulent kinetic energy, ϵ, and use dimensional analysis to arrive at

$$\tau_e(\boldsymbol{k}) \propto |\boldsymbol{k}|^{-\frac{2}{3}} \epsilon^{-\frac{1}{3}}. \tag{50}$$

Although somewhat simplistic, we will, going forward, assume

$$\tau_e(\boldsymbol{k}) = \tau_e(|\boldsymbol{k}|) = \frac{M}{\sqrt{\alpha_K}} |\boldsymbol{k}|^{-\frac{2}{3}} \epsilon^{-\frac{1}{3}}, \tag{51}$$

where the constant M is introduced, also outside the inertial subrange. The Kolmogorov constant has been included in (51) because we find it convenient to keep the quantity $\alpha_K \epsilon^{2/3}$ intact. We can now integrate (28) that, for $\mathrm{d}U_1/\mathrm{d}z > 0$, gives us

$$\Omega(\boldsymbol{k}_0, t - t_0) = \frac{\left(-k_{30} + \frac{\mathrm{d}U_1}{\mathrm{d}z} k_1 (t - t_0)\right)}{10 M \frac{\mathrm{d}U_1}{\mathrm{d}z} k_1} \left|\left(k_1, k_2, k_{30} - \frac{\mathrm{d}U_1}{\mathrm{d}z} k_1 (t - t_0)\right)\right|^{2/3}$$

$$\left(3 + 2\,{}_2\mathrm{F}_1\left(5/6, 1, 3/2, -\frac{\left(k_{30} - \frac{\mathrm{d}U_1}{\mathrm{d}z} k_1 (t - t_0)\right)^2}{k_1^2 + k_2^2}\right)\right) \sqrt{\alpha_K} \epsilon^{1/3}, \tag{52}$$

where $_2\mathrm{F}_1$ is the hypergeometric function. For $\mathrm{d}U_1/\mathrm{d}z \to 0$, we expect (52) to approach $\frac{t-t_0}{2\tau_e(\boldsymbol{k}_0)}$ plus an integration constant.

One way of determining the constant M would be to utilize that in the inertial subrange

$$\chi_{13}(k_1, 0) \to \iint_{\kappa_1 = k_1} \tau_e(\boldsymbol{\kappa})^2 \left(-\frac{1}{\tau_e(\boldsymbol{\kappa})} \frac{\mathrm{d}\,\widehat{R}_{13}^{\mathrm{ISO}}(\boldsymbol{\kappa}_0(0))}{\mathrm{d}t_0}\right.$$

$$\left. + \frac{\mathrm{D}\left\langle \eta_1(\boldsymbol{\kappa}_0, 0, 0) \,\overline{\eta_3(\boldsymbol{\kappa}_0, 0, 0)}\, \mathrm{d}^3\kappa\, \mathrm{d}t_0\right\rangle}{\mathrm{D}\,t}\right) \mathrm{d}^3\boldsymbol{\kappa}$$

$$\to \iint_{\kappa_1 = k_1} \frac{\mathrm{d}U_1}{\mathrm{d}z} \frac{5k_1^2 k_3^2 - 3k_2^2 |\boldsymbol{k}|^2}{12\pi |\boldsymbol{k}|^6} \tau_e(\boldsymbol{\kappa}) E(|\boldsymbol{\kappa}|)\, \mathrm{d}^3\boldsymbol{\kappa}$$

$$= -\frac{33}{1729} \frac{\mathrm{d}U_1}{\mathrm{d}z} \tau_e(k_1) E(k_1), \tag{53}$$

in which $\boldsymbol{\kappa}_0(t - t_0) = \left(\kappa_1, \kappa_2, \kappa_3 + \kappa_1 \frac{\mathrm{d}U_1}{\mathrm{d}z} (t - t_0)\right)$. Inserting the asymptotic behaviour of $\tau_e(k_1)$ and $E(k_1)$ we see that the right-hand side of (53) scales as $k_1^{-\frac{7}{3}} \epsilon^{1/3}$, which is consistent with observations (Wyngaard and Coté 1972). To remove its dependence on ϵ we can divide the square of $\chi_{13}(k_1, 0)$ with $\chi_{11}(k_1, 0)$, which correspondingly approaches $\frac{9}{55} k_1^{-\frac{5}{3}} \alpha_K \epsilon^{2/3}$. In Sect. 4 we follow this line of reasoning and investigate

$$M^*(k_1) = \sqrt{\frac{k_1^3\, \chi_{13}(k_1, 0)^2}{\chi_{11}(k_1, 0)}}\, \frac{1729}{33} \sqrt{\frac{9}{55}} \frac{\mathrm{d}U_1}{\mathrm{d}z}^{-1}, \tag{54}$$

where $M^*(k_1)$ consequently should approach M in the inertial subrange. Equation 54 thus indicates that studying the ratio between different components of the cross-spectra at known shear could be interesting in terms of determining M.

This section introduced an expression for the added energy due to newborn eddies, $N_{ij}(\boldsymbol{k}_0)$, as well as an expression for the eddy lifetime, $\tau_e(\boldsymbol{k})$. It can be argued that these expressions are on the simplistic side and that they should depend on, for example, R_{ij}. The counter argument would be that coupling the building blocks of the model to the end result in such a way would make the model significantly harder to evaluate. The section ended with implicitly suggesting an experiment for determining M (introduced in (51)), which is a key quantity of the framework.

3 Practical Application of the Models

3.1 Implementing the Spectral Velocity Tensor for $\tau = 0$

When implementing the spectral velocity tensor(s) it is convenient to introduce

$$G = \frac{M}{\sqrt{\alpha_K} \epsilon^{1/3}} \frac{\mathrm{d}U_1}{\mathrm{d}z} L_M^{2/3}, \tag{55}$$

which, for $\mathrm{d}U_1/\mathrm{d}z > 0$, enables us to write (51) as

$$\tau_e(\boldsymbol{k}) = G \frac{\mathrm{d}U_1}{\mathrm{d}z}^{-1} L_M^{-\frac{2}{3}} |\boldsymbol{k}|^{-\frac{2}{3}} \tag{56}$$

and (52) can then, for $G > 0$, be written as

$$\Omega(L_M, G, \boldsymbol{k}_0, \beta) = \frac{(-k_{30} + k_1\beta)}{10Gk_1} |(k_1, k_2, k_{30} - k_1\beta)|^{2/3}$$
$$L_M^{2/3}\left(3 + 2 \, _2\mathrm{F}_1\left(5/6, 1, 3/2, -\frac{(k_{30} - k_1\beta)^2}{k_1^2 + k_2^2}\right)\right) \tag{57}$$

with $\beta = \frac{\mathrm{d}U_1}{\mathrm{d}z}(t - t_0)$. This in turn allows us to write (25) as

$$\boldsymbol{B}(L_M, G, \boldsymbol{k}_0, \beta) = \mathrm{e}^{-(\Omega(L_M, G, \boldsymbol{k}_0, \beta) - \Omega(L_M, G, \boldsymbol{k}_0, 0))} \begin{bmatrix} 1 & 0 & \zeta_1(\boldsymbol{k}_0, \beta) \\ 0 & 1 & \zeta_2(\boldsymbol{k}_0, \beta) \\ 0 & 0 & |\boldsymbol{k}|^2/|(k_1, k_2, k_{30} - k_1\beta)|^2 \end{bmatrix} \tag{58}$$

with ζ_1 and ζ_1 still given by (26) and (27). We can now reformulate (41) for $\tau = 0$ and $\mathrm{d}U_1/\mathrm{d}z > 0$ according to

$$\widehat{R}_{ij}(\boldsymbol{k}, 0) = \int_{-\infty}^{t} B_{im}(\boldsymbol{k}_0, t - t_0) \frac{1}{\tau_e(\boldsymbol{k}_0)} \widehat{R}_{mn}^{\mathrm{ISO}}(\boldsymbol{k}_0) B_{jn}(\boldsymbol{k}_0, t - t_0) \, \mathrm{d}t_0$$
$$= \int_0^{\infty} B_{im}(L_M, G, \boldsymbol{k}_0, \beta) \frac{L_M^{2/3} |\boldsymbol{k}_0|^{2/3}}{G} \widehat{R}_{mn}^{\mathrm{ISO}}\left(\alpha_K \epsilon^{2/3}, L_M, \boldsymbol{k}\right) B_{jn}(L_M, G, \boldsymbol{k}_0, \beta) \, \mathrm{d}\beta$$
$$= \widehat{R}_{ij}\left(\alpha_K \epsilon^{2/3}, L_M, G, \boldsymbol{k}_0\right), \tag{59}$$

where $\boldsymbol{k}_0 = \left(k_1, k_2, k_3 + k_1 \frac{\mathrm{d}U_1}{\mathrm{d}z}(t - t_0)\right) = (k_1, k_2, k_3 + k_1\beta)$. In the last step of (59) we have introduced $\widehat{R}_{ij}\left(\alpha_K \epsilon^{2/3}, L_M, G, \boldsymbol{k}\right)$ for $G > 0$. For $G = 0$ (which corresponds to $\mathrm{d}U_1/\mathrm{d}z = 0$) we set

$$\widehat{R}_{ij}\big(\alpha_K\epsilon^{2/3}, L_M, 0, \boldsymbol{k}\big) = \widehat{R}_{ij}^{\text{ISO}}\big(\alpha_K\epsilon^{2/3}, L_M, \boldsymbol{k}\big), \tag{60}$$

with $\widehat{R}_{ij}^{\text{ISO}}$ given by (47). As $R_{ij}^{\text{L}}(\boldsymbol{x}, 0) = R_{ij}(\boldsymbol{x}, 0)$ it should come as no surprise that also $\widehat{R}_{ij}^{\text{L}}$ can be simplified to $\widehat{R}_{ij}\big(\alpha_K\epsilon^{2/3}, L_M, G, \boldsymbol{k}\big)$ for $\tau = 0$.

The spectral velocity tensor defined in (59) is closely related to the Mann (1994) tensor, which can similarly be written $\widehat{R}_{ij}\big(\alpha_K\epsilon^{2/3}, L_M, \Gamma, \boldsymbol{k}\big)$. The difference between the two tensors lies in how $\tau_e(\boldsymbol{k})$, which in Mann (1994) is given by

$$\tau_e(\boldsymbol{k}) = \Gamma \frac{dU_1}{dz}^{-1} \frac{|\boldsymbol{k}|^{-\frac{2}{3}} L_M^{-\frac{2}{3}}}{\sqrt{{}_2F_1\left(\frac{1}{3}, \frac{17}{6}, \frac{4}{3}, -|\boldsymbol{k}|^{-2} L_M^{-2}\right)}} \tag{61}$$

instead of (56), is combined with the rapid distortion equation. As previously mentioned, instead of decaying continuously, the eddies in Mann (1994) are subjected to rapid distortion according to their current age, which is set to exactly $\tau_e(\boldsymbol{k})$. This way of assigning a typical age to the eddies enables the Mann (1994) tensor to avoid the integration over eddy birth times seen e.g. in (41). As has been shown before and will be demonstrated again in Sect. 4.1, the Mann (1994) tensor performs very well for the case $\tau = 0$, despite its simplified approach to eddy decay.

Next, we consider the case $\tau \neq 0$, a situation in which the Mann (1994) tensor is not applicable.

3.2 Implementing the Spectral Velocity Tensor for $\tau \neq 0$

Using (29) and (59) we can simplify (41) to

$$\widehat{R}_{ij}\big(\alpha_K\epsilon^{2/3}, L_M, G, \boldsymbol{k}, \tau\big) = e^{-\frac{1}{2}\Theta^2(\boldsymbol{k}, \tau)} \, \widehat{R}_{im}\big(\alpha_K\epsilon^{2/3}, L_M, G, \boldsymbol{k}\big)$$
$$B_{jm}\left(L_M, G, \boldsymbol{k}, \frac{G\sqrt{\alpha_K}\epsilon^{1/3}}{ML_M^{2/3}}\tau\right), \tag{62}$$

where B_{ij} is given by (58), and where $\Theta(\boldsymbol{k}, \tau)$ is defined in (38). Though not clear from the notation, $\Theta(\boldsymbol{k}, \tau)$ depends also on $\alpha_K\epsilon^{2/3}$, L_M and G.

Equation 43 can analogously be simplified to

$$\widehat{R}_{ij}^{\text{L}}\big(\alpha_K\epsilon^{2/3}, L_M, G, \boldsymbol{k}, \tau\big) = e^{-\frac{1}{2}\Theta_{\text{L}}^2(\boldsymbol{k}, \tau)} \, \widehat{R}_{im}\big(\alpha_K\epsilon^{2/3}, L_M, G, \boldsymbol{k}\big)$$
$$B_{jm}\left(L_M, G, \boldsymbol{k}, \frac{G\sqrt{\alpha_K}\epsilon^{1/3}}{ML_M^{2/3}}\tau\right), \tag{63}$$

with Θ_{L} defined in (44).

Evaluating (62) or (63) for $\tau \neq 0$ can, however, be very computationally intensive. The reason is that, in the process, we evaluate (38) or (44), and then integrate (34) and (42), respectively, both of which in turn integrate (59). One solution to this problem is to first evaluate $\mathring{\chi}_{ij}\big(\alpha_K\epsilon^{2/3}, L_M, G, |\boldsymbol{k}|\big)$, defined in (5), for a range of $|\boldsymbol{k}|$ values and use interpolation in the resulting look-up table when evaluating (34), or (42). The look-up table can be calculated once and for all if the relationship

$$\widehat{R}_{ij}(1, 1, G, L_M\boldsymbol{k}) = \frac{\widehat{R}_{ij}\big(\alpha_K\epsilon^{2/3}, L_M, G, \boldsymbol{k}\big)}{\alpha_K\epsilon^{2/3}L_M^{11/3}}, \tag{64}$$

which leads to

$$\mathring{\chi}_{ij}\left(\alpha_K\epsilon^{2/3}, L_M, G, |\boldsymbol{k}|\right) = \alpha_K\epsilon^{2/3} L_M^{5/3} \mathring{\chi}_{ij}(1, 1, G, L_M|\boldsymbol{k}|), \tag{65}$$

is used and the look-up table is constructed in two dimensions, G and $L_M|\boldsymbol{k}|$.

Next, we discuss two different strategies for obtaining the necessary input information required to evaluate the presented models, an objective that, assuming knowledge of the constants α_K and M, is equivalent to finding suitable values of the parameters $\alpha_K\epsilon^{2/3}$, L_M and G.

3.3 Deriving Parameter Values from ϵ, u_* and dU_1/dz

Assuming knowledge of the rate of dissipation of turbulent kinetic energy, ϵ, the friction velocity, u_*, and the shear, dU_1/dz, then clearly $\alpha_K\epsilon^{2/3}$ is given directly by the rate of dissipation, ϵ, and the Kolmogorov constant, α_K. With the objective of deriving L_M and G from ϵ, u_* and dU_1/dz, we start by rearranging (55) to

$$M = \frac{G\sqrt{\alpha_K}\epsilon^{1/3}}{\frac{dU_1}{dz}L_M^{2/3}} \tag{66}$$

and multiplying both sides by $\frac{u_*^2 \frac{dU_1}{dz}}{\alpha_K^{3/2}\epsilon}$ to obtain

$$M\frac{u_*^2 \frac{dU_1}{dz}}{\alpha_K^{3/2}\epsilon} = \frac{G\sqrt{\alpha_K}\epsilon^{1/3}}{\frac{dU_1}{dz}L_M^{2/3}}\frac{u_*^2 \frac{dU_1}{dz}}{\alpha_K^{3/2}\epsilon} = \frac{Gu_*^2}{\alpha_K\epsilon^{2/3}L_M^{2/3}} = -G\iiint \widehat{R}_{13}(1, 1, G, \boldsymbol{\xi}) \, d^3\boldsymbol{\xi}, \tag{67}$$

where in the last step we have used (64). We note that the right-hand side of (67) is a function of G only. In Fig. 4, this quantity is displayed for a typical range of G. The left-hand side of (67) can be interpreted as the ratio between the shear production of turbulent kinetic energy, $u_*^2 dU_1/dz$, and the rate of dissipation of turbulent kinetic energy, ϵ, multiplied by a constant. As seen in Fig. 4, this ratio determines G uniquely.
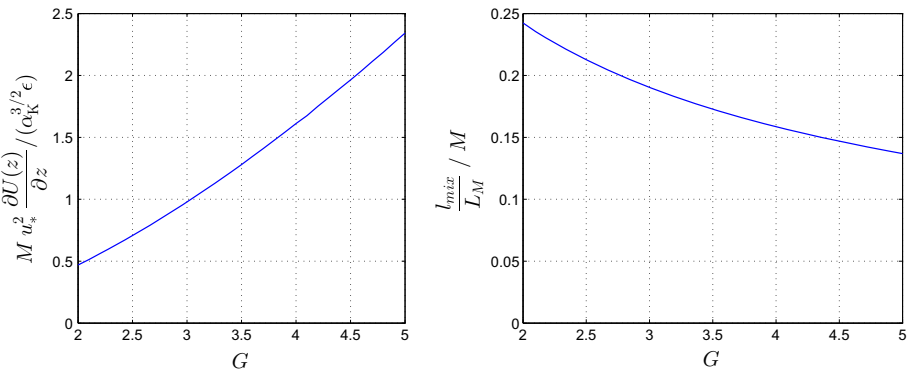
Fig. 4 To the left, the left-hand side of (67) versus G shows that G is uniquely determined by the ratio between the turbulent energy production from the shear gradient and the rate of dissipation of turbulent kinetic energy. To the *right*, the *left-hand* side of (69) divided by M shows that the ratio l_{mix}/L_M depends on G and thereby, also this quantity depends on the ratio between the turbulent energy produced from the shear gradient and the rate of dissipation

Having determined G, then L_M is given by (55) as

$$L_M = \frac{G^{3/2}\alpha_K^{3/4}\epsilon^{1/2}}{\frac{dU_1}{dz}^{3/2}M^{3/2}}. \tag{68}$$

Digressing slightly, we divide the definition of the mixing length, $l_{\text{mix}} = u_*/\frac{dU_1}{dz}$, with (68) and obtain

$$\frac{l_{\text{mix}}}{L_M} = \frac{u_*/\frac{dU_1}{dz}}{\left(\frac{G^{3/2}\alpha_K^{3/4}\epsilon^{1/2}}{\frac{dU_1}{dz}^{3/2}M^{3/2}}\right)} = \frac{M}{G}\sqrt{\frac{u_*^2\frac{dU_1}{dz}M}{G\alpha_K^{3/2}\epsilon}} = \frac{M}{G}\sqrt{-\iiint \widehat{R}_{13}(1,1,G,\boldsymbol{\xi})\,d^3\boldsymbol{\xi}}, \tag{69}$$

where in the last step we have used (67). In the right-hand graph of Fig. 4 we see how $\frac{l_{\text{mix}}}{L_M}/M$ depends on G.

In this section we have shown that knowledge of ϵ, u_* and dU_1/dz is sufficient to derive the necessary input information for the spectral velocity tensor. In the process we have also shown that both G and the ratio l_{mix}/L_M are given uniquely by the ratio between the shear production of turbulent kinetic energy, $u_*^2 dU_1/dz$, and the rate of dissipation of turbulent kinetic energy, ϵ.

3.4 Determining Parameter Values from Measured Spectra

For many applications the physical properties ϵ, u_* and dU_1/dz are not known, and it can be advantageous to use the alternative strategy outlined in Mann (1994), of measuring spectra and determining which set of tensor parameter values best reproduces the measured spectra.

Finding tensor parameters in this way requires repeated evaluation of (4), and with this in mind it may be beneficial to first produce a look-up table of $\chi_{ij}(1, 1, G, L_M k_1)$ and interpolate to find

$$\chi_{ij}(\alpha_K\epsilon^{2/3}, L_M, G, k_1) = \alpha_K\epsilon^{2/3} L_M^{5/3} \chi_{ij}(1, 1, G, L_M k_1). \tag{70}$$

In Fig. 5 this method is applied to spectra obtained at 80-m height and a wind speed of 16 m s^{-1} at Høvøre, Denmark, for neutral atmospheric stability. The resulting values of $\alpha_K\epsilon^{2/3}$, L_M and G are not identical to the closely related parameters of the Mann (1994) tensor $\alpha_K\epsilon^{2/3}$, L_M and Γ. However, the differences between the resulting parameter values of the two tensors are dwarfed by the uncertainty owing to the choices made in the fitting procedure, i.e. a small change in the fitting procedure would change the comparison result. The spectral velocity tensor fits the components of the measured spectra at least as well as the Mann (1994) tensor. We note that the spectral velocity tensor does not, at least in this example, over-predict the u_1u_3 cross-spectrum as is apparently the case using the Mann (1994) tensor, see Peña et al. (2010).

We have not taken into consideration the fact that the measured spectra in this case were not truly spatial spectra, but obtained using a stationary anemometer. The spectra corresponding to a stationary anemometer can be derived from $\widehat{R}(\boldsymbol{k}, \tau)$ by first calculating $R(\boldsymbol{x} - (\boldsymbol{U_0} + \boldsymbol{U(x)})\,\tau, \tau)$. This avenue is, however, not pursued here because it appears quite computationally intensive. When attempting this, one may keep in mind that x_1 of the spectral velocity tensor is not defined as aligned with the mean wind, $\boldsymbol{U_0} + \boldsymbol{U(x)}$, but with the direction of the shear, $d\boldsymbol{U}/dz$.
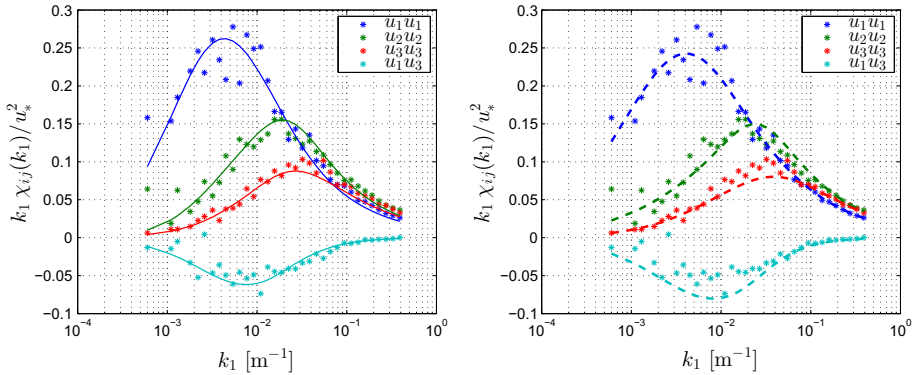
Fig. 5 Comparison of spatial spectra from the spectral velocity tensor (*left*) and the Mann (1994) tensor (*right*) for neutral stratification at $16\,\mathrm{m\,s^{-1}}$. The spectral velocity tensor fits the components of the measured spectra at least as well as the Mann (1994) tensor, and it does not, at least in this example, over-predict the $u_1 u_3$ cross-spectrum as Mann (1994) has been reported to do. The resulting parameters of the spectral velocity tensor versus the Mann (1994) tensor are $\alpha_K \epsilon^{2/3} = 0.070\,\mathrm{m^{4/3}s^{-2}}$ versus $\alpha_K \epsilon^{2/3} = 0.085\,\mathrm{m^{4/3}s^{-2}}$, $L_M = 63.3$ m vs. $L_M = 51.2$ m and $G = 3.46$ vs. $\Gamma = 3.49$. The experience so far is that the difference in the resulting parameters is smaller than the uncertainty incurred by the choices made when designing the fitting procedure

4 Validation

4.1 Lateral and Longitudinal Coherence

To investigate the spectral velocity tensor's ability to predict coherences, we turn to data from LES performed on a $600 \times 600 \times 400$ cell mesh with a resolution of $4 \times 4 \times 2.5$ m. We choose data from a height of 100 m of a neutrally stratified simulation, and here we define x_1 as being parallel to $\mathrm{d}U/\mathrm{d}z$. For more information regarding the LES, see Sullivan and Patton (2011) and Berg et al. (2013).

Given that we have access to whole planes of data we can calculate spatial spectra, and in Fig. 6 we have determined the parameter values of the spectral velocity tensor that best reproduces the LES spatial spectra. The resulting values, $\alpha_K \epsilon^{2/3} = 0.0085\,\mathrm{m^{4/3}s^{-2}}$, $L_M = 57.7$ m and $G = 3.23$, together with $\mathrm{d}U_1/\mathrm{d}z = 0.0083\,\mathrm{s^{-1}}$ correspond to $M = 2.40$. Determining M from the parameters resulting from the fitting of measured spectra was attempted in de Maré and Mann (2014) in which the value $M = 3$ was proposed, however, the uncertainty using this methodology is considerable. Perhaps a better way of determining M is to use (54), and this method is demonstrated in the right-hand frame of Fig. 6 where the LES results indicate a higher value than the afore-mentioned M value of 2.40. Using LES to determine M in this way is, however, not ideal owing to the finite resolution of the calculation grid. Therefore, we recommend using $M = 3$ for now; however, based on the above considerations the uncertainty in this value is currently 20 % or more.

It is worth mentioning that, with the look-up table of $\chi_{ij}(1, 1, G, L_M k_1)$ mentioned in Sect. 3.4, it is straightforward to verify the formal manipulations of (53) (which is the basis for (54)). If the derivation is correct then the quantity $G^{-1} k_1^{7/3} L_M^{7/3} \chi_{13}(1, 1, G, L_M k_1)$ should, according to (53) combined with (51), (66) and (70), approach $-33/1729$ in the inertial sub-range.
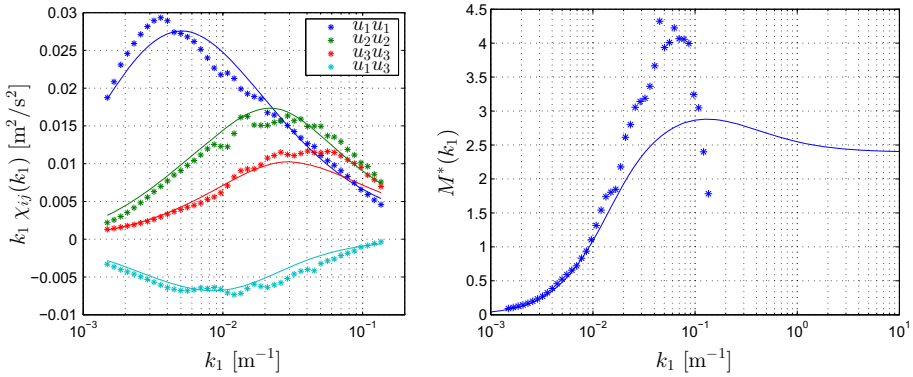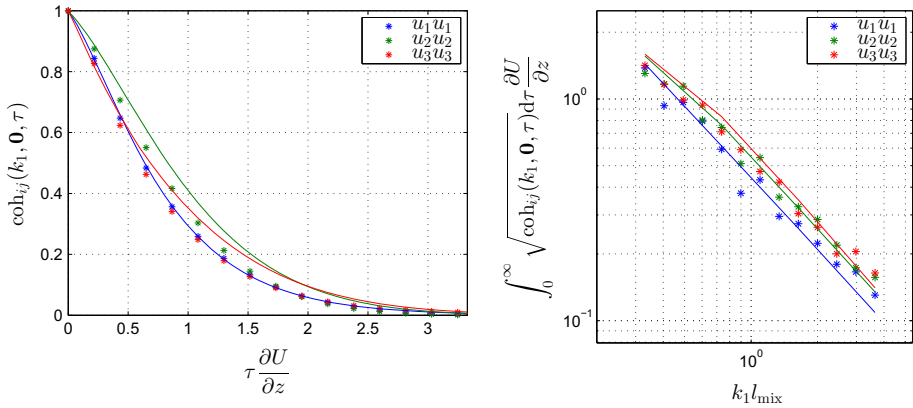
Fig. 6 To the *left*, fitting the spectral velocity tensor to LES spatial spectra, resulting in parameter values: $\alpha_K \epsilon^{2/3} = 0.0085\,\mathrm{m}^{4/3}\mathrm{s}^{-2}$, $L_M = 57.7\,\mathrm{m}$ and $G = 3.23$. To the *right*, an attempt to determine M using (54), where, as we recall, the quantity, M^*, is expected to approach M asymptotically in the inertial subrange. The *solid line* shows the quantity in question using the spectral velocity tensor with the set of parameter values resulting from the afore-mentioned spectral fitting. As expected, the *curve* approaches the value given by (66) for high values of k_1. The corresponding LES results indicates a higher trajectory than the *solid line*, before trailing off, presumably due to the finite resolution of the calculation grid
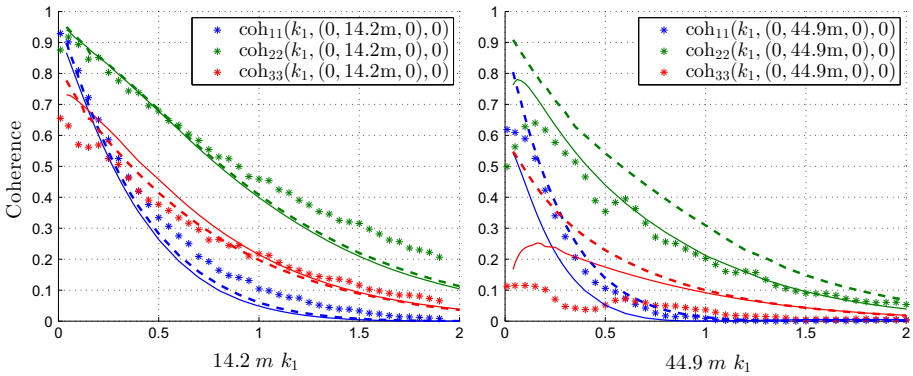

Fig. 7 To the *left*, lateral coherence, $\mathrm{coh}_{ij}(k_1, \boldsymbol{r}, 0)$ for $\boldsymbol{r} = (0, 14.2\,\mathrm{m}, 0)$. Both the spectral velocity tensor (*solid lines*) and the Mann (1994) tensor (*dashed*) perform well for this distance. To the *right*, the same quantity for $\boldsymbol{r} = (0, 44.9\,\mathrm{m}, 0)$. The Mann (1994) tensor performs better for the streamwise component (*blue*), whereas the situation is reversed for the transversal component (*green*). Both tensors overpredict the vertical component (*red*)

In Fig. 7, to the left, we compare lateral coherence, $\mathrm{coh}_{ij}(k_1, \boldsymbol{r}, 0)$, for $\boldsymbol{r} = (0, 14.2\,\mathrm{m}, 0)$ derived from the spectral velocity tensor with the same quantity extracted from the LES data. The right-hand graph of Fig. 7 shows the same quantities for $\boldsymbol{r} = (0, 44.9\,\mathrm{m}, 0)$. In the graphs of Fig. 7, lateral coherence derived from the Mann (1994) tensor is shown for comparison, and it is found that the new spectral velocity tensor performs on par with the Mann (1994) tensor. Both tensors overpredict coherence for the vertical component at separations larger than $0.5 L_M$ in the lateral direction. Coherence in the vertical direction is not addressed at this point, as the lack of homogeneity makes this direction less straightforward. When addressing such coherences, the methodology of Mann (1994) can be used as inspiration.

Fig. 8 To the *left*, longitudinal coherence derived from the spectral velocity tensor (*solid lines*) for $k_1 = 0.33/l_{\text{mix}} = 0.71/L_M$ is compared to the same quantity extracted from the LES data. To the *right*, an integral time scale constructed from the longitudinal coherence. The value of k_1 in the left-hand frame corresponds to the left-most *dot*(s) in the right-hand frame
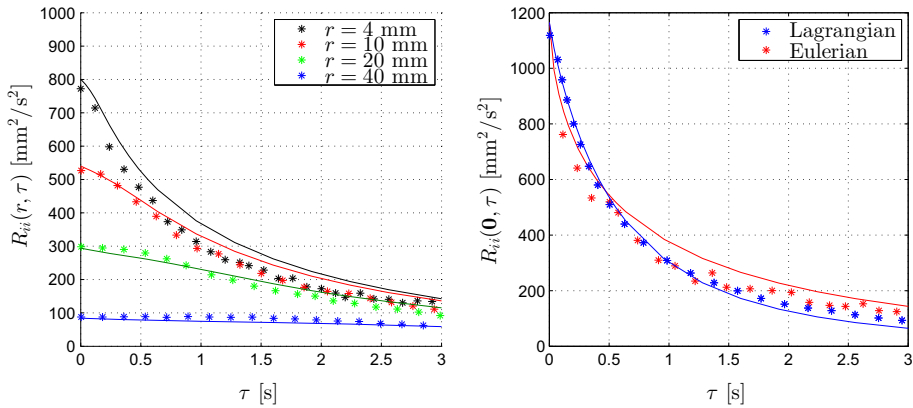
Fig. 9 Sum of covariances for all three components derived from the spectral velocity tensor (*solid lines*) compared to measured results for isotropic turbulence presented in Ott and Mann (2005). To the *left*, Eulerian covariance for various separations in space and time. To the *right*, a comparison between the Eulerian and the Lagrangian covariance for $r = 0$. We see that our model reproduces the crossover of $R_{ii}^{\text{L}}(\mathbf{0}, \tau)$ and $R_{ii}(\mathbf{0}, \tau)$ at approximately half the maximum value, a behaviour also reported in Fung et al. (1992)

In Fig. 8, to the left, we compare the longitudinal coherence, $\text{coh}_{ij}(k_1, \mathbf{0}, \tau)$, derived from the spectral velocity tensor with the same quantity extracted from the LES data, for $k_1 = 0.33/l_{\text{mix}} = 0.71/L_M$. The Mann (1994) tensor is not included in the graphs because, combined with the Taylor assumption of frozen turbulence, it would predict $\text{coh}_{ij}(k_1, \mathbf{0}, \tau) = 1$ for all time lags. The right-hand graph of Fig. 8 shows an integral time scale constructed as $\int_0^\infty \sqrt{\text{coh}_{ij}(k_1, \mathbf{0}, \tau)} \, \mathrm{d}\tau$.

4.2 Eulerian and Lagrangian Two-Point Correlations in Isotropic Turbulence

We also compare the performance of the spectral velocity tensor and its Lagrangian counterpart perform relative to measured results for isotropic turbulence presented in Ott and Mann

(2005). In Fig. 9, we see the Eulerian covariance, $R_{ii}(\boldsymbol{r}, \tau)$, for different separations $\boldsymbol{r}$ and τ, as well as the Lagrangian covariance, $R_{ii}^{\mathrm{L}}(\boldsymbol{0}, \tau)$, and the Eulerian covariance, $R_{ii}(\boldsymbol{0}, \tau)$. Both quantities are predicted significantly better than by any of the models presented in Ott and Mann (2005).

The cross-over point of the Eulerian and Lagrangian covariances, seen in the right-hand graph of Fig. 9, is sensitive to the choice of expression for R_k, see (33). As seen in the Figure, the chosen expression predicts a cross-over at approximately half the maximum value, a behaviour reported in e.g Fung et al. (1992) and Ott and Mann (2005). For comparison, no cross-over point is predicted if one of the alternative expressions mentioned in Sect. 2.3, is used instead. In the evaluation of the models we have used $\mathrm{d}U_1/\mathrm{d}z = 0$, $\alpha_{\mathrm{K}}\epsilon^{2/3} = 0.00622$ $\mathrm{m}^{4/3}\mathrm{s}^{-2}$, $L_M = 0.0273$ m and $M = 3$.

5 Conclusions

A spectral velocity tensor has been developed to predict all two-point correlations in space and time in sheared homogeneous turbulence. This was accomplished by combining the design philosophies behind two existing models, the Mann spectral velocity tensor, in which isotropic turbulence is distorted according to rapid distortion theory, and Kristensen's longitudinal coherence model, in which eddies are simultaneously advected by larger eddies as well as decaying. The model is built on simplified physics and assumptions such as that *eddies created at different times are uncorrelated*, and that *larger eddies displace smaller eddies as if the smaller eddies were shaped like spheres*. Assumptions such as these can be challenging to validate directly, and are here instead seen as indirectly validated by the prediction capabilities of the resulting model.

The model requires values of three parameters, $\alpha_{\mathrm{K}}\epsilon^{2/3}$, L_M and G, as input. It was shown that these values can be derived from the following physical properties of the flow: the rate of dissipation of turbulent kinetic energy, ϵ, the friction velocity, u_*, and the shear, $\mathrm{d}U_1/\mathrm{d}z$. Alternatively, the values of the input parameters can, as with the closely related parameters of the Mann (1994) tensor, be derived from measured spectra.

The resulting model predicts spatial correlations comparable to the Mann (1994) tensor and temporal coherence better than any of the models evaluated in Ott and Mann (2005). As part of the framework, a spectral velocity tensor for Lagrangian correlations in space and time is also developed and validated versus measurements of isotropic turbulence. Combined, the models reproduce the cross-over point between Eulerian and Lagrangian temporal covariances. As per the scope of the validation, the developed models can be used, for example, in wind-turbine engineering applications such as lidar-assisted feed forward control and wind-turbine wake modelling.

Future work might include experiments to better determine the introduced quantity M. An experiment with this objective, studying the ratio between different components of the cross-spectra at known shear, is implicitly proposed in Sect. 2.5. Other developments could include investigating the implications of using a rapid distortion formulation that also includes, e.g., buoyancy effects.

References

Batchelor GK (1953) The theory of homogeneous turbulence. Cambridge University Press, Cambridge, UK, pp 28–33

Berg J, Mann J, Patton EG (2013) Lidar-observed stress vectors and veer in the atmospheric boundary layer. J Atmos OceanTechnol 30(9):1961–1969. doi:10.1175/JTECH-D-12-00266.1

Bossanyi E, Savini B, Iribas M, Hau M, Fischer B, Schlipf D, van Engelen T, Rossetti M, Carcangiu CE (2012) Advanced controller research for multi-MW wind turbines in the UPWIND project. Wind Energy 15(1):119–145. doi:10.1002/we.523

Bossanyi E (2013) Un-freezing the turbulence: application to LiDAR-assisted wind turbine control. IET Renew Power Gener 7(4):321–329

Chougule AS (2013) Influence of atmospheric stability on the spatial structure of turbulence. DTU Wind Energy PhD-0028 (EN)

Chougule A, Mann J, Segalini A, Dellwik E (2014) Spectral tensor parameters for wind turbine load modeling from forested and agricultural landscapes. Wind Energy 18(3):469–481. doi:10.1002/we.1709

de Maré M, Mann J (2014) Validation of the Mann spectral tensor for offshore wind conditions at different atmospheric stabilities. J Phys Conf Ser 524(1):12,106

Fung JCH, Hunt JCR, Malik NA, Perkins RJ (1992) Kinematic simulation of homogeneous turbulence by unsteady random Fourier modes. J Fluid Mech 236:281–318. doi:10.1017/S0022112092001423

Hanazaki H, Hunt JCR (2004) Structure of unsteady stably stratified turbulence with mean shear. J Fluid Mech 507:1–42. doi:10.1017/S0022112004007888

Hunt JCR, Wray AA, Buell JC (1987) Big whorls carry little whorls. In: Proceedings of the 1987 Summer Program,CTR-S87 NASA Centre for Turbulence Research

Kaneda Y, Ishida T (2000) Suppression of vertical diffusion in strongly stratified turbulence. J Fluid Mech 402:311–327

Kolmogorov AN (1968) Local structure of turbulence in an incompressible viscous fluid at very high Reynolds numbers. Soviet Physics Uspekhi 10(6):734

Kristensen L (1979) On longitudinal spectral coherence. Boundary-Layer Meteorol 16(2):145–153. doi:10.1007/BF02350508

Larsen GC, Madsen HA, Thomsen K, Larsen TJ (2008) Wake meandering: a pragmatic approach. Wind Energy 11(4):377–395. doi:10.1002/we.267

Mann J (1994) The spatial structure of neutral atmospheric surface-layer turbulence. J Fluid Mech 273:141–168. doi:10.1017/S0022112094001886

Mikkelsen T, Angelou N, Hansen K, Sjöholm M, Harris M, Slinger C, Hadley P, Scullion R, Ellis G, Vives G (2013) A spinner-integrated wind lidar for enhanced wind turbine control. Wind Energy 16(4):625–643. doi:10.1002/we.1564

Moffatt K (1967) Interaction of turbulence with strong wind shear. In: Yaglom AM, Tatarski VI (eds) Atmosphere turbulence and radio wave propagationAtmosphere turbulence and radio wave propagation. Nauka, Moscow, pp 139–156

Ott S, Mann J (2005) An experimental test of Corrsin's conjecture and some related ideas. New J Phys 7(1):142

Pao LY, Johnson KE (2011) Control of wind turbines. IEEE Control Syst 31(2):44–62

Peña A, Gryning SE, Mann J (2010) On the length-scale of the wind profile. Q J R Meteorol Soc 136(653):2119–2131. doi:10.1002/qj.714

Pope SB (2000) Turbulent flows. Cambridge University Press, Cambridge, UK, pp 219–223

Saffman PG (1963) An approximate calculation of the Lagrangian auto-correlation coefficient for stationary homogeneous turbulence. Appl Sci Res Sect A 11(3):245–255. doi:10.1007/BF03184983

Salhi a, Cambon C (2010) Stability of rotating stratified shear flow: an analytical study. Phys Rev E 81(2):026,302

Sathe A, Mann J (2013) A review of turbulence measurements using ground-based wind lidars. Atmos Meas Tech 6(11):3147–3167. doi:10.5194/amt-6-3147-2013

Schlipf D, Cheng PW, Mann J (2013) Model of the correlation between lidar systems and wind turbines for lidar-assisted control. J Atmos OceanTechnol 30:2233

Simley E, Pao LY, Frehlich R, Jonkman B, Kelley N (2014) Analysis of light detection and ranging wind speed measurements for wind turbine control. Wind Energy 17(3):413–433. doi:10.1002/we.1584

Sullivan PP, Patton EG (2011) The effect of mesh resolution on convective boundary layer statistics and structures generated by large-eddy simulation. J Atmos Sci 68(10):2395–2415. doi:10.1175/JAS-D-10-05010.1

Townsend AA (1976) The structure of turbulent shear flow, 2nd edn. Cambridge University Press, Cambridge, UK, pp 88–91

von Kármán T (1948) Progress in the statistical theory of turbulence. Proc Nail Acad Sci 34(11):530–539

Wilczek M, Stevens RJAM, Narita Y, Meneveau C (2014) A wavenumber-frequency spectral model for atmospheric boundary layers. J Phys Conf Ser 524(1):12,104

Wilczek M, Narita Y (2012) Wave-number-frequency spectrum for turbulence from a random sweeping hypothesis with mean flow. Phys Rev E 6(86):066,308

Wyngaard JC, Coté OR (1972) Cospectral similarity in the atmospheric surface layer. Q J R Meteorol Soc 98(417):590–603. doi:10.1002/qj.49709841708